Momentum-resolved spectroscopy for the saddle-point excitons in InSb

Hiroshi Tanimura [1] and Katsumi Tanimura [2]
[1] *Institute for Materials Research, Tohoku University, 2-1-1 Katahira, Sendai 980-8577, Japan*
[2] *The Institute of Scientific and Industrial Research, Osaka University, 8-1 Mihogaoka, Ibaraki, Osaka 567-0047, Japan*

(Received 4 August 2020; revised 30 October 2020; accepted 19 November 2020; published 8 December 2020)

We use time- and angle-resolved photoemission spectroscopy to reveal momentum-resolved characteristics of interband transitions in InSb. The transitions along the Γ-*K* line are correctly described in terms of the independent-quasiparticle band picture up to 1.9 eV. However, the transitions along the Γ-*L* line turn out to be strongly excitonic above 1.7 eV, associated with the saddle-point excitons at the E_1 critical point. The momentum- and energy-resolved spectra of photoionization of the saddle-point excitons show that the wave function is composed of the electron-hole pair states with the wave vector of $0.453 \pm 0.055\,\text{Å}^{-1}$ along the Γ-*L* direction of the Brillouin zone. Time-resolved characteristics of the exciton photoionization show that the coherently generated excitonic polarization decays with a time constant of 22 ± 1 fs due to the autoionization from the excitonic state to uncorrelated electron-hole pair states.

DOI: 10.1103/PhysRevB.102.235202

I. INTRODUCTION

The optical spectra of semiconductors provide a rich source of information about their electronic properties [1,2]. In experimental optical spectra of semiconductors, energies, intensities, and spectral line shapes differ significantly from those predicted by the independent-quasiparticle picture (IQP) not only near the band-gap region at the M_0-type critical point, but also in the higher-energy regions around the M_1- and M_2-type critical points of Van Hove singularities in joint density of states (JDOS) for conduction and valence bands [1–4]. As is well known, the excitonic effect of many-body interaction in electronic systems is the key concept to correct the discrepancies and to gain a deeper understanding of the optical properties of solids.

The excitonic effect at the M_0 critical point near the Γ point, which forms distinctive excitonic absorptions below the band-gap energy E_G (the Γ excitons hereafter), have been studied extensively. Not only the spectroscopic characteristics, but also ultrafast dynamics of dephasing and scattering processes of the coherent excitonic polarization have been studied, and detailed knowledge of the Γ-exciton dynamics has been obtained [5–8].

The excitonic effects at the higher-energy region above E_G have also been studied for a long time. The imaginary parts of the dielectric functions $\epsilon(\omega)$ of diamond- and zinc-blende-type semiconductors increase above E_G to the first intense peaks (the E_1 transitions). The E_1 transitions have been attributed to the transitions related to the M_1 (saddle-type) critical points along the Λ direction of the Brillouin zone based on band-structure calculations [1,3,4,9–13]. The experimental line shape of the E_1 transitions deviates qualitatively from that expected for M_1 critical points of Van Hove singularities [1]. Based on extensive theoretical studies to elucidate the effect of Coulomb interaction between electron and hole at the M_1 critical point, the discrepancies have been explained by the excitonic effects at the critical points [1,9]. Such excitons occurring at saddle points in JDOS are known as the saddle-point excitons (SPEs) [3] or hyperbolic excitons [1], and the characteristic line shapes have been interpreted in terms of Fano interference [12,14,15]. Based on extensive optical study in a broad spectral range, it has been reported that the SPEs are formed also in graphene, a prototypical example of two-dimensional materials [16,17].

Theoretically, excitonic effects on the optical spectra of real materials have been studied from first principles [18–22]. Extensive calculations of excitonic effects on the dielectric functions have largely corrected the discrepancies between theoretical and experimental $\epsilon(\omega)$ spectra in many crystals, substantiating the important roles of excitonic effects in the high-energy region above E_G. Experimentally, however, the methods to study excitonic effects in the high-energy region were limited to the line-shape analysis of $\epsilon(\omega)$. Because of this limitation, fundamental properties of SPEs are still left unclarified in many crystals. In particular, the wave function of SPEs and the interaction between this high-energy excitonic state and the continuum of unbound electron-hole pair states are important issues to be explored.

An excitonic state is a superposition of electron-hole pair excitations with amplitude $f(\vec{k}_e, \vec{k}_h)$, where $\vec{k}_e$ and $\vec{k}_h$ are wave vectors of the electron and hole in IQP band structure [2,23]. For SPEs, the pair-excitation states that contribute most strongly to $f(\vec{k}_e, \vec{k}_h)$ are those around the momentum region of a Van Hove singularity [24]. Therefore, the precise experimental determination of the wave vectors for the E_1 critical points is important to elucidate the excitonic effects associated with the singularities. As the $\epsilon(\omega)$, which is essentially the *momentum-integrated* quantity, does not give any direct information on the location of a Van Hove singularity in the momentum space, introducing momentum-resolved spectroscopic methods is crucial for further studies of SPEs [25].

Recently, time- and angle-resolved photoemission spectroscopy (TR-ARPES) has been introduced to overcome the methodological limitations for studying high-energy excitons in GaAs [25]. TR-ARPES has a powerful capability of revealing momentum-resolved characteristics of interband transitions. In addition to this, recent theoretical studies of exciton photoionization [24,26–29] have emphasized a unique capability of TR-ARPES to obtain a deeper insight into the wave functions of excitons, as briefly summarized in the next section. Using TR-ARPES, important features of electronic structure and of dynamics of SPEs have been revealed for GaAs, a prototypical direct-gap semiconductor [25]. In this paper, we study, using TR-ARPES, the momentum-resolved characteristics of interband transitions in order to examine the high-energy excitonic effects in InSb, another model crystal showing the electronic properties characteristic of narrow-gap semiconductors.

InSb has the band-gap energy of 170 meV [30], and shows the E_1 transition at 1.85 eV at room temperature [10,31]. The energies are lower by about 1 eV than those in GaAs. Also, the high-frequency dielectric constant (15.7) is larger than that (10.9) of GaAs [32], giving a significant difference in the screening effect for carriers. Therefore, InSb is one of the best samples to study comparatively the importance of SPEs in the optical spectra in semiconductors. The excitonic effects on the E_1 transition in InSb have been studied for a long time [13,31,33], but the experimental evidence for the excitonic effects, obtained by line-shape analysis, is controversial; opposite conclusions have been reached even by the same method of analyzing the second derivative spectra of $\epsilon(\omega)$ [13,31].

Here we excite InSb crystals with pump-photon energy $h\upsilon_{\text{pump}}$ ranging from 1.18 to 1.88 eV, and the photoinduced excited electronic states are probed using angle-resolved photoemission spectroscopy (ARPES). We find that the independent-quasiparticle band picture gives correct descriptions of the transitions along the Γ-K line up to 1.9 eV, while the transitions along the Γ-L line turn out to be strongly excitonic above 1.7 eV, associated with the saddle-point excitons at the E_1 critical point at 1.85 eV. Based on time-, momentum-, and energy-resolved characteristics of exciton photoionization, we obtain far deeper insight into the dynamics and electronic structures of the SPE in InSb.

II. TR-ARPES AND THE PHOTOIONIZATION OF EXCITONS

In ARPES for electronic-structure determinations of solids, one assumes a definite initial one-electron energy level $E_{\text{IQP}}(\vec{k})$ from which electrons are photoionized ($\vec{k}$ being the wave vectors). Then, the direct information of energy and wave vector of the $E_{\text{IQP}}(\vec{k})$ can be obtained by measuring angle- and energy-resolved photoelectrons. The method can be applied to study the momentum-resolved characteristics of interband transitions using pump and probe techniques with ultrashort light pulses [34]. Pump pulses initially create the excitation with a well-defined phase relationship within the excitation and with the electromagnetic field that created the excitations. After the destruction of coherence through dephasing on a femtosecond timescale, nonthermal electrons are injected in the conduction band (CB) at a given $\vec{k}$ and generate holes with $-\vec{k}$ in the valence band (VB), governed by the energy and momentum conservations for the optical transitions [5–8]. The process of interband transitions can be probed by photoemission spectroscopy introducing probe-light pulses at a given time delay Δt with respect to pump-light pulses by the two-photon photoemission (2PPE) scheme. The electrons injected in the CB generate photoelectrons specified by the momentum $\hbar\vec{k}$ and the kinetic energy $E_K(\vec{k})$. The momentum-resolved information about the photoelectrons gives directly the wave vectors at which pump-induced interband transitions take place. The relation between $E_K(\vec{k})$ and $E_{\text{IQP}}(\vec{k})$ referenced to the valence band maximum (VBM) is given by

$$E_K(\vec{k}) = h\upsilon_{\text{probe}} + E_{\text{IQP}}(\vec{k}) - \Phi_{\text{vac}}, \tag{1}$$

where $h\upsilon_{\text{probe}}$ is the probe-photon energy and Φ_{vac} is the ionization energy. Thus the momentum-resolved characteristics of interband optical transitions can be captured by TR-ARPES.

However, such an initial one-electron energy level is indefinite for photoionization of excitons, although the exciton itself has a well-defined energy level and a momentum [24,26–29]. In the Wannier model, applicable for most inorganic semiconductors, an excitonic state $|\text{ex}\rangle$ with its center-of-mass wave vector $\vec{K} = 0$ is given by a superposition of various electron-hole pair excitations as [2,23]

$$|\text{ex}\rangle = \sum_{\vec{k}} f(\vec{k}, -\vec{k})\hat{a}^+_{\vec{k}}\hat{b}^+_{-\vec{k}}|0\rangle, \tag{2}$$

where $\hat{a}^+_{\vec{k}}$ and $\hat{b}^+_{-\vec{k}}$ are creation operators of an electron with wave vector $\vec{k}$ and of a hole with wave vector $-\vec{k}$ in the IQP electronic structure, and $|0\rangle$ is the vacuum state.

In the photoionization processes of excitons, only electrons are emitted out of crystals, while the conjugate holes are left inside, and recoiled back to "original" valence-band states with the recoil energy $E_R(-\vec{k})$. Under momentum and energy conservations, the photoemitted electron from an excitonic state has the momentum $\hbar\vec{k}$ and the energy $E_K(\vec{k})$ which is given by

$$E_K(\vec{k}) = h\upsilon_{\text{probe}} + E_{\text{EX}} - E_R(-\vec{k}) - \Phi_{\text{vac}}, \tag{3}$$

where E_{EX} is the excitonic-state energy referenced to the VBM [24,27]. Therefore, the recoil of conjugate holes plays crucial roles in the photoionization of excitons. More importantly, the photoemission intensity, specified by $\hbar\vec{k}$ and $E_K(\vec{k})$, is proportional to $|f(\vec{k}, -\vec{k})|^2$ such that angle-resolved photoemission spectroscopy directly measures the amplitudes of momentum- and energy-resolved IQP Bloch functions of which the excitonic states are composed [24,26–29]. Therefore, TR-ARPES makes it possible, in principle, to determine experimentally the correlation between an excitonic state and the IQP Bloch states responsible for the excitonic state.

As $E_R(-\vec{k})$ is determined primarily by the valence-band dispersion [24,27], the $E_K(\vec{k})$ in the exciton photoionization has no direct correlation with the conduction-band dispersion

$E_{\mathrm{IQP}}(\vec{k})$ of the IQP picture. Also, the momentum distribution of photoelectrons is governed by the exciton wave function itself, and is not related directly to the dispersion of $E_{\mathrm{IQP}}(\vec{k})$. When any excitonic effects are weak enough at a given critical point, the initial state of photoemission lies on the $E_{\mathrm{IQP}}(\vec{k})$ predicted by the IQP band structure in the energy and momentum spaces. However, when excitonic effects are strong at a given critical point, the pump pulses generate the excitonic polarization, and the photoemission process is governed by the exciton-photoionization scheme, which generates photoelectrons with $\hbar\vec{k}$ and $E_K(\vec{k})$ specific to the excitonic state. In fact, $\hbar\vec{k}$ and $E_K(\vec{k})$ in the photoionization of the SPEs in GaAs deviate strongly from those predicted by the $E_{\mathrm{IQP}}(\vec{k})$ [25]. Therefore, TR-ARPES provides a powerful method to capture excitonic effects in the interband transitions at a given critical point.

III. EXPERIMENT

Nondoped InSb (100) wafers with thickness of 3 mm were cleaved under ultrahigh-vacuum conditions ($<5\times10^{-11}$ Torr). Surface structures were characterized *in situ* by a scanning tunneling microscope prior to photoemission measurements [35]. The (110) surfaces displayed well-ordered (1×1) structure with linear In and Sb rows, and with a surface-defect concentration less than 0.5%. We used two different femtosecond (fs) laser systems. A mode-locked Ti:sapphire laser, operated at a 76 MHz repetition rate, was used to generate fs-laser pulses between 830 and 760 nm. The fundamental and its third harmonic, generated using beta-barium borate (BBO) crystals, were used as pump and probe pulses. The temporal widths of the pump and the probe pulses were 70 and 75 fs, respectively, giving a cross-correlation trace of 105 fs (full width at half maxima) in a BBO crystal. To generate laser pulses with shorter temporal widths and wider tunability, we also used a laser system consisting of a Ti:sapphire laser oscillator, a regenerative amplifier, and a tunable optical parametric amplifier operated at 250-kHz repetition rate. The optical parametric amplifier generated 40-fs laser pulses at photon energies tunable from 1.18 to 2.30 eV. A part of the amplified fundamental output at 795 nm was used to generate the third harmonic with a temporal width of 50 fs, giving a cross-correlation trace of 64 fs (full width at half maxima). The probe pulses passed a computer-controlled delay stage with a high precision to set the time delay (Δt) with respect to the pump pulses, and pump and probe pulses were aligned coaxially and focused on the sample surfaces at 45° to surface normal. The pump-pulse fluence was set to give a typical excitation density ρ_0 of $5\pm1\times10^{17}\,\mathrm{cm}^{-3}$, which was evaluated using the formula $\rho_0 = F_p(1-R)\alpha$, with the photon fluence of pump pulse F_p, the reflectivity R, and the absorption coefficient α at $h\upsilon_{\mathrm{pump}}$. The probe-pulse fluence was typically less than 1/500 of the pump-pulse fluence. Using a hemispherical electron analyzer operated in an angle-resolved lens mode, equipped with a two-dimensional image-type detector, photoelectron images were recorded as a function of the $E_K(\vec{k})$ and emission angle θ along the [001] crystal direction: Surface normal photoemission was along the [110] crystal direction. The energy resolution using fs-probe light was 75 meV, while the angle resolution was ±0.5°. All measurements were made at 293 K.

In time-resolved photoemission measurements, the final state energies reached by pump and probe pulses were limited to below 6.6 eV with respect to the Fermi level. The inelastic mean free path at the energy region is typically 30 Å [36], which is substantially larger than the depth of the (1×1) surface layer of ∼1 Å [37]. Therefore, the bulk sensitivity is enhanced strongly, compared with normal ultraviolet photoemission spectroscopy probed by light with photon energy of typically a few tens of eV. The $E_K(\vec{k})$ of a photoelectron was referenced to the low-energy cutoff in a photoemission spectrum which corresponds to the vacuum level of a sample [38]. For InSb (110)-(1×1) surfaces, $\Phi_{\mathrm{vac}} = 4.84\pm0.06\,\mathrm{eV}$ [37]. As the $E_K(\vec{k})$ is dependent on $h\upsilon_{\mathrm{probe}}$, we use the energy $E_I(\vec{k})$ of an initial state of photoemission, defined as $E_I(\vec{k}) = E_K(\vec{k}) + \Phi_{\mathrm{vac}} - h\upsilon_{\mathrm{probe}}$, when we compare the spectra measured with different $h\upsilon_{\mathrm{probe}}$. The $E_I(\vec{k})$ was referenced to the CBM, not to the VBM. One reason is that we could determine the energy of the conduction-band minimum (CBM) precisely in the photoemission spectra. Furthermore, when we compare experimental results with theoretical band-structure calculations, this quantity becomes more convenient, as the band-structure calculations do not give the band-gap energy at 293 K.

IV. EXPERIMENTAL RESULTS

A. Momentum-resolved characteristics of interband transitions in the photoemission map

Figure 1(a) shows the energy- and momentum-resolved (k-resolved) maps of photoemissions measured at $\Delta t = 30$ fs under excitation with $h\upsilon_{\mathrm{pump}}$ at 1.26 eV. In the figure, photoemission intensities specified by color scales are plotted as a function of electron momentum ($k_{||}$) parallel to the surface and the initial-state energy $E_I(\vec{k})$ for photoemission referenced to the CBM. The experimental geometry of photoemission measurements is shown in Fig. 1(b). The [110] crystal axis is aligned along the surface normal, and the [110] and [001] axes define the detection plane. Under this geometry, the bulk Brillouin zone (BBZ) and the surface Brillouin zone (SBZ) have the relation shown in Fig. 1(c) [35,39]. As the emission angle corresponds to $k_{||}$ along the $\bar{\Gamma}-\bar{Y}$ $(=\bar{X}')$ direction of the SBZ, the measured photoemission image represents a one-dimensional cut, along $\bar{\Gamma}-\bar{Y}$ of the SBZ, of the two-dimensional projection of three-dimensional electron distributions. The projection has the following characteristics. First, all states along the Γ-K direction in the BBZ are projected at $\bar{\bar{\Gamma}}$, contributing to surface-normal photoemission. Second, the states along the Γ-L line in the BBZ are projected on the $\bar{\Gamma}-\bar{Y}$ direction with $k_{||}$ given by $k_{||} = k_L\cos(54.7^\circ)$, with k_L being the wave vector along the Γ-L direction. Third, the states along the Γ-X line in the BBZ are projected on the $\bar{\Gamma}-\bar{Y}$ direction with $k_{||} = k_X$, with k_X being the wave vector along the Γ-X direction.

Figure 1(d) shows the IQP band structure calculated using GW and the screened hybrid functional in Ref. [40]. The solid (broken) curve in Fig. 1(a) is the CB dispersion along the Γ-L direction (Γ-X direction) as a function of $k_{||}$. As

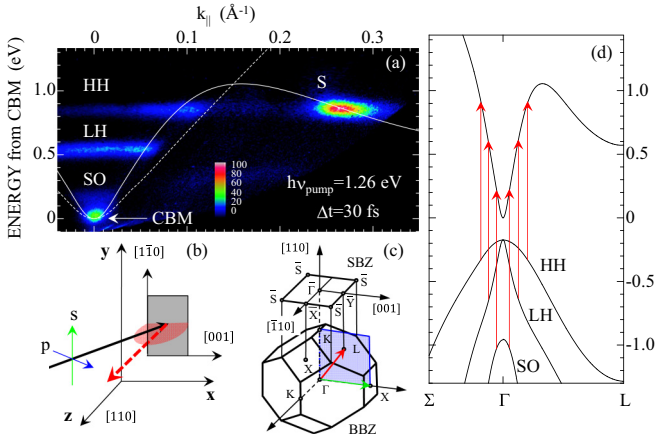

FIG. 1. (a) Photoemission image 30 fs after excitation with *s*-polarized 1.26-eV light pulses. Photoemission intensities specified by the color scale are plotted as a function of electron momentum ($k_{||}$) parallel to the surface and initial-state energy referenced to the CBM. The solid and broken curves show the conduction-band dispersion along Γ-*L* and Γ-*X* directions, plotted as a function of $k_{||}$, based on the band-structure calculation in Ref. [40]. (b) Experimental geometry of photoemission measurements. The [110] crystal axis is aligned along the surface normal, and the [110] and [001] axes define the detection plane. (c) The relation between the surface Brillouin zone and bulk Brillouin zone for InSb with (110) surface under the geometry shown in (b). The plane (light blue) is the projection plane, and the red (green) arrow within the plane shows the direction from the Γ to *L* (Γ to *X*) points. (d) Part of the band structure of InSb (Ref. [40]). Energy is referenced to the conduction-band minimum, and the band-gap energy is set to be the experimental value (0.17 eV) at 293 K. Red arrows show typical optical transitions for 1.26-eV photons.

is well known, the determination of $k_{||}$ fixes a point on the two-dimensional SBZ; the momentum $k_{\perp}$ normal to the surface can have a value anywhere along the rod extending into the three-dimensional BBZ [39]. Therefore, the off-normal photoemission detected experimentally at a given $k_{||}$ is a superposition of many contributions from such states that are projected on the one-dimensional cut along the $\bar{\Gamma} - \bar{Y}$ direction of the SBZ. Despite the composite features in off-normal emission, it is instructive to compare the result with the CB dispersion along the Γ-*L* line to which theoretical studies have given the quantitative dispersion characteristics [40,41]. Under the experimental geometry given in Fig. 1(b), the states along the Γ-*L* line contribute to off-normal emissions from typical high-symmetry points. As the $k_{\perp}$ is zero for states along the Γ-*X* direction, they cannot be detected under the geometry; the curve along the Γ-*X* line in Fig. 1(a) portrays the border of a low-energy part of the Γ valley.

The maximum of the first CB along the Γ-*L* direction is located at $k_L = 0.275\,\text{Å}^{-1}$ ($k_{||} = 0.16\,\text{Å}^{-1}$) in this calculation. Therefore, photoemissions with $k_{||} < 0.16\,\text{Å}^{-1}$ come from electrons photoinjected into the Γ valley of the CB, while those with $k_{||} > 0.16\,\text{Å}^{-1}$ originate from the states outside the Γ valley. In the present configuration shown in Fig. 1(b), the states at the high-energy side of the *L* valley contribute to the photoemissions at the range $k_{||} > 0.169\,\text{Å}^{-1}$; the L_1 point of the CB corresponds to $k_{||} = 0.485\,\text{Å}^{-1}$, being outside of our detection window.

In Fig. 1(a), the initial-state populations in the Γ valley are characterized by three stripes labeled HH, LH, and SO. As described above, the photoemissions at surface normal ($k_{||} = 0$) come from the states along the Γ-*K* line. In Fig. 1(d), typical optical transitions are indicated by red arrows. The interband optical transitions from the heavy-hole (HH), light-hole (LH), and split-off (SO) valence bands to the CB states along the Γ-*K* line predict the energies of final states of optical transitions (or of the initial states of photoemission), which are in reasonable agreement with the peaks labeled HH, LH, and SO. For the transitions along the Γ-*L* line, we have similar energies of final states of optical transitions because of similar dispersive characteristics of VB and CB bands in the energy range. Therefore, we can conclude that the three peaks are due to electrons with nonthermal distributions in the CB injected by the transitions from HH, LH, and SO valence bands [35].

In Fig. 1(a), there is one intense photoemission peak, labeled *S*, in the *L*-valley region ($k_{||} = 0.25\,\text{Å}^{-1}$). The peak *S* is specified by the same initial-state energy as that of HH peak in the Γ valley. The origin of the peak *S* has been identified in Ref. [35] as being caused by the electrons in the *L* valley transferred from the Γ valley by ultrafast intervalley scattering. The identification has been based on the analysis of rise times of photoemission peaks; the rise time of peak *S* is the same as the decay time of the HH peak. Because of the ultrafast rates of Γ-*L* intervalley scattering and of the finite temporal widths of pump- and probe-light pulses, it cannot be excluded to detect photoemissions from the secondary states, which are defined as the states populated by the scattering processes of the primary states generated by photoexcitation. However, based on the rise-time analysis using the time-resolved capability of TR-ARPES, it is possible to distinguish clearly the photoemissions from the primary and secondary states (see Ref. [35] and the Appendix). Ultrafast relaxation dynamics of photoinjected electrons in the CB in InSb have been studied extensively in Ref. [35]. In this paper, we pay attention to the energy- and momentum-resolved characteristics of photoemission peaks from the primary states of optical transitions.

B. Primary-state photoemissions as a function of pump-photon energy

Figure 2 compares the photoemission maps measured at $\Delta t = 30$ fs for $h\upsilon_{\text{pump}}$ ranging from 1.49 to 1.88 eV. The map under 1.49-eV excitation shows essentially the same features as those at 1.26 eV shown in Fig. 1(a). On the other hand, the photoemission patterns at higher-energy excitations exhibit significant changes depending on $h\upsilon_{\text{pump}}$. Characteristic features of the changes in photoemission patterns can be summarized as follows. First, there are stripelike signals in the Γ valley ($k_{||} < 0.16\,\text{Å}^{-1}$) for all cases, although the intensities become weak with increasing $h\upsilon_{\text{pump}}$. Second, for $h\upsilon_{\text{pump}} \geqslant 1.77$ eV, the photoemission is featured by one intense peak, labeled EX, at $k_{||} = 0.268\,\text{Å}^{-1}$ and $E_I(\vec{k}) = 0.83$ eV. The EX peak is detected even under $h\upsilon_{\text{pump}} = 1.72$ eV as shown in Fig. 2(d). Third, in the intermediate range between 1.55 and

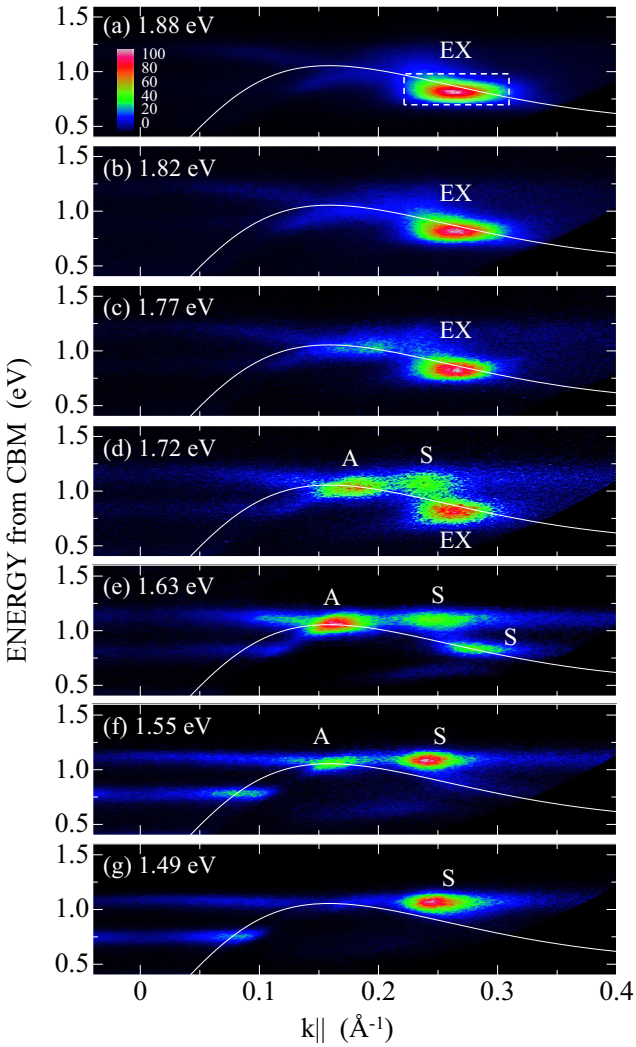

FIG. 2. Photoemission images, measured at $\Delta t = 30$ fs, plotted as a function of $k_{||}$ and $E_I(\vec{k})$ under excitation with photon energies ranging from 1.49 to 1.88 eV. The solid curve in each panel displays the CB dispersion along the Γ-L line. In each panel, photoemission intensities are normalized to the highest-intensity peak in order to display multiple-peak features clearly [the color scale in (a) is common]. The $h\upsilon_{\text{pump}}$-dependent changes in photoemission intensities of typical peaks are described in Fig. 3. For the labels EX, A, and S, see the text.

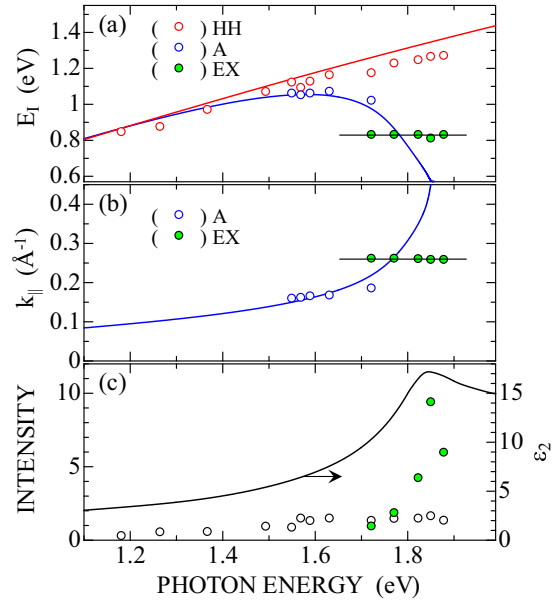

FIG. 3. The initial-state energy (a) and the peak $k_{||}$ (b) of the photoemission peaks due to the primary states of interband transitions at $h\upsilon_{\text{pump}}$ ranging from 1.19 to 1.88 eV. The red and blue curves show the theoretical predictions for transitions from the HH valence band to the CB along the Γ-K and Γ-L lines. In (c), the intensity of the EX peak at $\Delta t = 30$ fs, integrated within a rectangle shown in Fig. 2(a), is plotted by green circles as a function of $h\upsilon_{\text{pump}}$. The black open circles show the total intensity of photoemission generated by the transitions from the HH valence band (excluding the EX peak). The results obtained under the excitation density of $5 \pm 1 \times 10^{17}$ cm^{-3} are compiled. The solid curve in (c) is the imaginary part of $\epsilon(\omega)$ at 300 K [31].

1.72 eV, an additional peak labeled A can be detected around the saddle point of the CB. At $h\upsilon_{\text{pump}} = 1.63$ eV, the peak A is the most intense photoemission peak.

As shown in the Appendix, where temporal changes were extensively analyzed for the result under 1.63-eV excitation, the peak A, generated under excitation from 1.55 to 1.72 eV, is due to a primary state of optical transition; it shows a fast rise to have the maximum at $\Delta t < 30$ fs, similar to the HH peak in the Γ valley. Peaks labeled S in Figs. 2(d)–2(g) are due to secondary states which show delayed rises, similar to that under 1.26-eV excitation. The EX peak, generated at $h\upsilon_{\text{pump}} > 1.70$ eV, is another primary state of optical transitions as shown later.

In Fig. 3, we summarize $h\upsilon_{\text{pump}}$-dependent changes in the initial-state energy, the magnitude of $k_{||}$ that gives the peak (peak $k_{||}$ hereafter), and the intensities of photoemission peaks. The red and blue curves in Fig. 3(a) show the theoretical initial-state energies predicted for the transitions from the HH valence band to CB along the Γ-K and Γ-L lines based on the band structure shown in Fig. 1(d). The $E_I(\vec{k})$ of the HH peak at $k_{||} = 0$ increases almost linearly with increasing $h\upsilon_{\text{pump}}$. The $h\upsilon_{\text{pump}}$-dependent increase of $E_I(\vec{k})$ agrees reasonably well with the theoretical prediction of the interband transitions from the HH band to CB along the Γ-K line. Similarly, the $E_I(\vec{k})$ of peak A, which is roughly constant, agrees well to the theoretical prediction of the interband optical transitions along the Γ-L line. Not only the $E_I(\vec{k})$ but also the peak $k_{||}$ for peak A is well registered on the theoretically predicted dispersion curve as seen in Fig. 3(b). Therefore, we can conclude that the peak A is due to the electrons injected by the optical transitions from the HH valence band to the CB along the Γ-L line.

On the other hand, the EX peak is characterized by the constant $E_I(\vec{k})$ of 0.83 eV and the constant peak $k_{||}$ of 0.26 Å^{-1}, irrespective of $h\upsilon_{\text{pump}}$ ranging from 1.72 to 1.88 eV. In this energy range, theoretically predicted $E_I(\vec{k})$ and peak $k_{||}$ change sensitively, reflecting characteristic dispersions of the CB and HH valence bands along the Γ-L line. The theoretical features

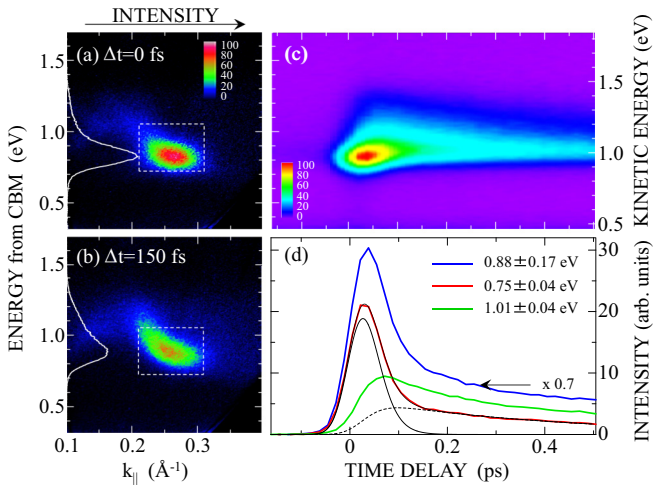

FIG. 4. (a), (b) Part of photoemission map and angle-integrated (0.21–0.32 Å^{-1}) photoemission spectrum measured at $\Delta t = 0$ (a) and at $\Delta t = 150$ fs (b) under 1.82-eV excitation. (c) Temporal evolution of angle-integrated photoemission spectra. The right-axis scale represents the kinetic energy of photoelectrons. (d) Temporal evolution of photoemission intensities integrated with respect to parallel momentum (0.21–0.32 Å^{-1}) and energy. Blue, red, and green curves show the intensities integrated with energy widths indicated in the panel. Black curves are the results of quantitative analysis (see the text).

are not specific to the results in Ref. [40], as the results obtained by different theoretical methods show essentially the same features [41]. Therefore, it is evident that the EX peak has an origin different from other photoemission peaks that can be ascribed to the electrons photoinjected by the VB-to-CB transitions in the BBZ spanned by the Γ-K and Γ-L lines.

In Fig. 3(c), the intensity of the EX peak at $\Delta t = 30$ fs is plotted by green circles as a function of $h\upsilon_{\rm pump}$. The EX peak is excited for $h\upsilon_{\rm pump} > 1.70$ eV, and the largest enhancement occurs at $h\upsilon_{\rm pump} = 1.85$ eV. The solid curve in Fig. 3(c) is the imaginary part of $\epsilon(\omega)$ at 300 K [31]. It is clear that the EX peak is excited resonantly at the E_1 transition energy. The black open circles in the figure show the total intensity of photoemission generated by the transitions from the HH valence band (excluding the EX peak). Photoemission intensities not only due to primary states but also those due to secondary states associated with the HH peaks were summed up to determine the total intensity. The intensity increases with increasing $h\upsilon_{\rm pump}$, but the EX-peak excitation becomes the most dominant channel of optical transitions around the E_1 transition energy.

C. Temporal evolution of the EX photoemission peak

The EX peak shows a very unique feature in the "relaxation process." In Figs. 4(a) and 4(b), we show the map of photoemission measured at $\Delta t = 0$ fs and 150 fs under 1.82-eV excitation. Not only the intensity but also the dispersive features of the peak change significantly in this short time frame. The white curves in the figures are the angle-integrated photoemission spectra in the range from 0.21 to 0.32 Å^{-1}. The peak is at $E_I(\vec{k}) = 0.83$ eV at $\Delta t = 0$ fs, while the peak shifts to 0.89 eV at $\Delta t = 150$ fs; the peak energy of the EX photoemission displays collectively a *high-energy shift* during relaxation. Figure 4(c) shows temporal evolution of angle-integrated spectra displayed two dimensionally as a function of $E_I(\vec{k})$ and Δt. It is clear that the ultrafast spectral change associated with a high-energy shift takes place within 100 fs, leaving the component characterized by a slower decay rate. The ultrafast relaxation associated with a high-energy shift is contrasted strongly to the relaxation of nonthermal electrons in the CB as shown in Ref. [35] and the Appendix.

In Fig. 4(d), the energy- and angle-integrated intensity within the rectangle in Fig. 4(a), specified by $E_I(\vec{k})$ ranging from 0.71 to 1.05 eV and $k_{||}$ from 0.21 to 0.32 Å^{-1}, is plotted as a function of Δt. The integrated intensity reaches the maximum at $\Delta t = 30$ fs, and the decay is bimodal. In order to make the temporal changes clearer, we plotted the intensities integrated at a low-energy part (0.71–0.78 eV) and at a high-energy part (0.98–1.05 eV) by red and green curves, respectively. In view of a high-energy shift of the photoelectrons, the former represents more clearly the dynamics of the fast component, while the latter represents that of the slow component, although both of them are overlapped partially. It is clear that the fast component decays within 100 fs of excitation, and that the slow component grows when the fast component decays. Therefore, the state responsible for the low-energy photoemission, which is the primary state of optical transitions, is transferred to the secondary state which is responsible for the photoemission at high-energy sides. We analyze the temporal changes in intensity quantitatively later in order to make the physics involved in the unique feature of the EX-peak relaxation clear.

We carried out similar time- and angle-resolved photoemission measurement under 1.82-eV excitation using a different sample orientation where the detection plane is defined by the [110] and [1$\bar{1}$0] axes (see Fig. 1). In this case, off-normal emissions are characterized by $k_{||}$ along the $\bar{\Gamma} - \bar{X}$ direction of the SBZ, to which the states along the Γ-X direction in the BBZ contribute with $k_{||} = k_X \sin(45^\circ)$. However, we could not detect any intense peaks, similar to the EX photoemission, for the $k_{||}$ ranging from 0 to 0.38 Å^{-1}. Therefore, the state responsible for the EX photoemission (the EX state hereafter) is highly localized in the two-dimensional plane of the BBZ defined by axes of [110] and [001], which includes the states along the Γ-L direction of the BBZ.

V. DISCUSSION

As described in Sec. IV, the EX-photoemission peak dominates over other features in the photoemission from InSb excited at $h\upsilon_{\rm pump} > 1.7$ eV. The EX peak is characterized by a constant $k_{||}$ (0.26 Å^{-1}) and constant $E_I(\vec{k})$(=0.83 eV), irrespective of $h\upsilon_{\rm pump}$ ranging from 1.72 to 1.88 eV. The momentum- and energy-resolved characteristics of the EX peak deviate completely from the predictions based on the interband transitions in the IQP picture. The EX state is highly localized in the momentum space in the two-dimensional plane of the BBZ defined by axes of [110] and [001], and shows ultrafast temporal evolution. The formation yield of the EX state is excitation-wavelength dependent, and the resonant

enhancement occurs at $h\upsilon_{\text{pump}} = 1.85$ eV which corresponds to the E_1 transition energy. The photoemission peak that has essentially the same characteristics as those of the EX peak in InSb has been reported for GaAs recently [25]. For GaAs, the EX state has been identified as the saddle-point excitons associated with the E_1 transition at 2.95 eV. Here we argue that the EX photoemission in InSb is also due to the SPE associated with the E_1 critical point, based on quantitative analysis of results obtained above.

A. Energy- and momentum-resolved characteristics of EX photoemission

Recent theoretical studies on exciton photoionization have revealed several important aspects which differ significantly from those for the one-electron photoemission scheme [24,26–29], as briefly summarized in Sec. II. Here we examine critically the relation between the present results and the theoretical consequences of exciton photoionization. For the SPEs in diamond- and zinc-blende-type semiconductors, it has been shown theoretically that not only the electron-hole pair states along the Γ-L direction, but also those along the two transverse directions perpendicular to the Γ-L direction contribute to the wave function significantly [1,9]. In the present study, however, the measurement of k-resolved photoemission is restricted only along the $\bar{\Gamma} - \bar{Y}$ direction of the SBZ; no results are available for two transverse directions. Nevertheless, the results provide crucial information on the electronic structure of the SPE in InSb.

In Fig. 5(a), we show the photoemission map at $\Delta t = 0$ fs under 1.85-eV excitation as a function of E_K and $k_{||}$. Based on the ultrafast temporal changes in the EX photoemission shown in Fig. 4, the spectrum at this time delay has been particularly chosen to analyze spectral line shapes of the primary state of photoexcitation. The energy scale is given by the kinetic energy of photoelectrons, as the initial-state energy given by the IQP picture has no physical meaning in the case of the exciton photoionization process [see Eq. (3)]. Although the photoemissions from photoinjected conduction electrons may be present, together with the EX photoemission, the intensities are rather weak. Therefore, it is possible to analyze quantitatively the spectral shape of the fast component of the EX photoemission with the least ambiguity.

The photoemission spectrum at the peak $k_{||}(=0.262\ \text{Å}^{-1})$, shown in Fig. 5(b), is characterized by the peak kinetic energy at 0.98 eV. As will be described in the next section, the decay time of the fast component of EX photoemission is 22 ± 1 fs, which corresponds to energy broadening of 30 meV. Therefore, we calculated the Lorentzian line shape with this width and convolved it with respect to a finite experimental energy resolution of 75 meV. The thin solid black curve in Fig. 5(b) is the result of this convolution, showing reasonable agreement with the experimental spectrum. The exciton-photoionization theory predicts the photoelectron-kinetic energy given by Eq. (3). The important role of hole restoration inducing the recoil energy $E_R(-\vec{k})$ is schematically shown in Fig. 5(d). When we identify the $E_{\text{EX}} = 1.85$ eV, which is the photon energy giving the peak for EX-photoemission excitation shown in Fig. 4(c), the recoil energy $E_R(-\vec{k})$ by the hole restoration

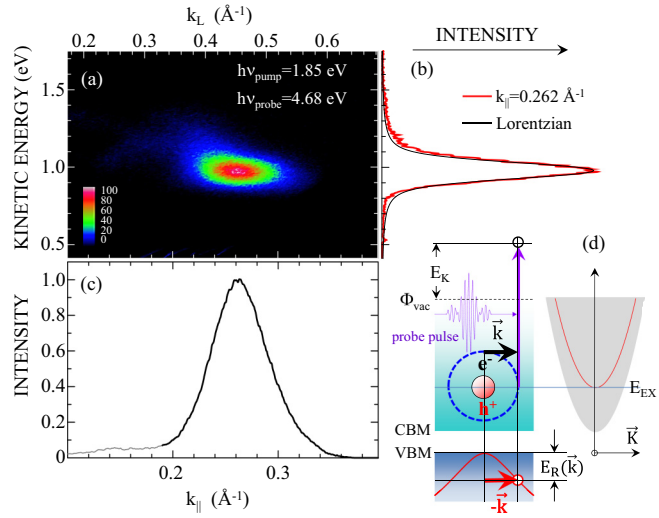

FIG. 5. (a) Part of photoemission map measured at $\Delta t = 0$ under 1.85-eV excitation plotted as a function of $k_{||}$ and the kinetic energy of photoelectrons. (b) Photoemission spectrum at $k_{||}$=0.262 Å^{-1} of the image in (a). The black curve shows a theoretical Lorentzian spectrum with a lifetime broadening of 30 meV (seen the text). (c) The momentum-resolved intensity of energy-integrated EX photoemission in (a). The intensity at $k_{||} < 0.19$ Å^{-1} is due to hot electrons in the CB. (d) A schematic diagram of the photoionization process of excitons. The right panel shows the ground and excited states in a two-particle picture with the exciton state shown by the red curve. An electron is photoionized with a momentum $\hbar\vec{k}$ from an exciton by a probe pulse, while the conjugate hole restores the valence-band state with the recoil energy $E_R(-\vec{k})$.

is evaluated to be 0.71 ± 0.06 eV; the error range is originated from the fluctuation of reported magnitudes of Φ_{vac} [37].

In the sudden approximation of photoemission [42], $E_R(-\vec{k})$ is determined by the dispersion relation of the valence band [24,27]. The dispersion of HH valence band along the Γ-L direction may contribute primarily to the $E_R(-\vec{k})$. No experimental results have been reported for the valence-band dispersions along the Γ-L direction for InSb. However, theoretically it has been reported that the HH valence-band state is lower in energy by 0.72 ± 0.01 eV at $k_{||} = 0.262$ Å^{-1} ($k_L = 0.453$ Å^{-1}) than the VBM [40,41]. The magnitude of $E_R(-\vec{k})$ obtained by Eq. (3) is in a reasonable range expected from the valence-band dispersion. Therefore, the exciton-photoionization theory describes well one of the characteristics of EX photoemission, substantiating our conclusion that the EX photoemission is due to the exciton photoionization.

In the photoionization of excitons with $\vec{K} = 0$, the photoemission intensity specified by $\hbar\vec{k}$ and E_K is proportional to $|f(\vec{k}, -\vec{k})|^2$ [24,26–29]. The spectrum in Fig. 5(c) shows the energy-integrated and momentum-resolved photoemission intensity as a function of $k_{||}$. In order to exclude possible inclusions of photoemission components from conduction electrons, only the low-energy half of the spectrum was integrated. The maximum is at $k_{||} = 0.262$ Å^{-1} with a width (full width at half maxima) of 0.060 Å^{-1}. In view of important roles of the IQP Bloch states along the Γ-L direction

on the SPE formation, we may correlate the distribution of k-resolved photoemission intensity to the states along the Γ-L direction. The k_L that corresponds to $k_{||}$ is plotted as the upper scale of Fig. 5(a); $k_{||} = 0.262\,\text{Å}^{-1}$ corresponds to $k_L = 0.453\,\text{Å}^{-1}$. Therefore, the electron-hole pair states at $k_L = 0.453 \pm 0.055\,\text{Å}^{-1}$ are primarily involved in the SPE wave function.

As is well known, when a semiconductor is excited by ultrashort laser pulses with a broadband nature at the exciton resonance, the light field induces an optical polarization that is directly proportional to the exciton wave function [5,43,44]. In the present study, we have captured the excitonic polarization in the 2PPE scheme by introducing ultrashort probe-light pulses [29]. In view of the short time frame of measurement around $\Delta t = 0$ and the short lifetime of EX photoemission mentioned below, the wave function we discussed above represents an ensemble average of the SPE states involved in the polarization. As stated above, electron-hole pair states along the two transverse directions perpendicular to the Γ-L line also play important roles in the SPE formation [1,9]. Adding experimental results for these states, using more sophisticated imaging techniques in TR-ARPES [45], will provide comprehensive knowledge for the IQP Bloch states of which the SPE wave function is composed.

B. Dynamical properties of the saddle-point exciton

Based on the conclusion we have reached in Sec. V A that the EX photoemission is due to the photoionization of SPEs, we discuss the dynamical properties of the SPE, an excitonic state formed at energy higher than E_G. In Fig. 4, it is clear that the primary product of photoexcitation is the low-energy component of the EX peak; the high-energy component is generated as a result of the decay of the fast component. In order to gain more quantitative information on the dynamics of the SPEs, we first analyze the decay characteristics. The semiconductor Bloch equations certainly provide a suitable theoretical framework for analyzing optical properties of semiconductors [5,46]. However, here we use a simple optical Bloch equation with neglecting all Coulomb interaction terms in the semiconductor Bloch equations [47]. We obtain only phenomenological quantities of population decay time T_1 and polarization dephasing time T_2.

The exciton photoionization process is modeled in terms of two sequential excitation steps [25,48]: The first step is the resonance excitation from the ground state $|1\rangle$ to the excitonic state $|2\rangle$, and the second one is exciton photoionization leading to the final state $|3\rangle$ at which the electron is photoemitted. In this model, $T_2 = 2T_1$ [48]. In the analysis, we calculate population of the state $|2\rangle$ using a simple optical Bloch equation, and the second photoionization step is evaluated by simply convoluting the results of the state $|2\rangle$ with probe pulses. For the bimodal decay of EX photoemission, the fast component was analyzed by the optical Bloch equation to determine the population decay time T_1, and the slow component was described by a rate equation with the population rise time being the same as the T_1 for the fast component [25,34]. The results of the analysis are displayed and compared with experimental results in Fig. 4(d). The solid black curve shows the fast component for $T_1 = 22\,\text{fs}$, while the broken curve shows the slow component of the EX photoemission for a decay time constant τ of 400 fs. The sum of two components, shown by a thin solid black curve, describes well the experimental results. We confirmed that experimental decay of the EX photoemission is best described by $T_1 = 22 \pm 1\,\text{fs}$ and $\tau = 400 \pm 10\,\text{fs}$, based on the analysis of results obtained under excitation with different photon energies ranging from 1.72 to 1.88 eV.

As is well known in previous time-resolved spectroscopy, the dephasing processes in semiconductors are carrier-density dependent [6,7,49]. In order to examine the effects of excitation density on the population decay time determined above, we analyzed the results of EX-photoemission obtained for ρ_0 ranging from 5.0×10^{17} to $2.0 \times 10^{18}\,\text{cm}^{-3}$. In this excitation-density range, the intensity of the EX photoemission increased in proportion to ρ_0, while the decay times of both fast and slow components did not show any density-dependent changes; they showed the same magnitudes within the error range described above. The results reveal that the dephasing process of coherent excitonic polarization associated with SPEs is not affected strongly by the carrier-density dependent scattering processes in the excitation range studied, and suggest that the dephasing is governed by other interactions of SPEs.

For the Γ excitons formed below E_G in semiconductors, the decay of resonantly excited macroscopic polarization is governed by the dephasing time typically in the picosecond range, and dephasing leads to incoherent populations of excitons [5]. On the other hand, the coherent excitonic polarization associated with the SPE decays with a short time constant of 22 fs. An excitonic state far above E_G is the bound state immersed in the continuum of uncorrelated electron-hole pair states with high density of states, resulting in the strong interaction between the discrete and continuum states [15]. Therefore, the coherent excitonic polarization may be transferred into unbound pair states with a rate dependent on the strength of the electronic interaction. We presume that the fast decay of the EX photoemission corresponds to the process of "autoionization" [15], or the transfer from the coherently formed excitonic state to unbound electron-hole pair states.

In the electronic process of conversion from excitonic states to unbound electron-hole pair states, the screening of electron-hole attraction caused by the corrective response of the photogenerated electron-hole plasma may play important roles [50,51]. The collective behavior of Coulomb screening is a retarder response, as clearly demonstrated by ultrafast time-resolved terahertz spectroscopy [52,53]; the time delay of the Coulomb screening is the order of the inverse plasma frequency ω_{pl}. As mentioned above, the effects of ρ_0 on the magnitude of T_1 of the EX photoemission were examined for ρ_0 ranging from 5.0×10^{17} to $2.0 \times 10^{18}\,\text{cm}^{-3}$. When we assume that all absorbed photons generate a nonequilibrium plasma [54], $2\pi/\omega_{pl}$ changes from 74 to 37 fs depending on ρ_0, which are in a similar time range as the T_1. However, the magnitude of T_1 does not depend on ρ_0, indicating that the collective behavior of Coulomb screening does not play significant roles in the autoionization process of SPEs.

The growth of the slow component of EX photoemission is governed by the decay of SPEs. This slow component can be ascribed to the energetic electrons generated by the autoionization of excitons, and the decay, characterized by a time

constant of 0.4 ps, represents the relaxation of the nonthermal electrons at the L valley. As shown in Fig. 4, the slow component is featured by the higher kinetic energy of photoelectrons compared to that of the fast component, leading to an unusual high-energy shift in relaxation process. However, as described in Sec. II, the kinetic energy of photoelectrons in the IQP picture and that in the exciton photoionization are determined by different rules. When the photoemission process changes from exciton photoionization to the ionization of electrons with high excess energies in the CB, the physical meaning of kinetic energies of photoelectrons may change accordingly. Therefore, we presume that the apparent high-energy shift of the kinetic energy of photoelectrons during the relaxation process shown in Fig. 4 reflects the time-dependent change in photoemission mechanisms; the exciton photoionization process which is dominant at $\Delta t < 100$ fs is replaced by the photoionization of nonthermal electrons in the CB at $\Delta t > 100$ fs.

By the autoionization of the SPEs into the uncorrelated electron-hole pair states, the electrons with nonthermal distribution and high excess energies are generated in the CB. The distribution of thus formed nonthermal electrons may depend strongly on the wave function of the SPE and the details of the autoionization mechanism. As revealed in Ref. [35], the relaxation of photoinjected electrons in the CB of InSb is complex; not only the energy relaxation due to electron-phonon interaction, but also the impact ionization due to electron-electron interaction play an important role in the relaxation process. Elucidation of the details of the autoionization process and the relaxation pathways of nonthermal electrons generated from SPEs at highly excited states in the CB will be interesting future issues.

VI. SUMMARY

We have studied the momentum-resolved characteristics of interband optical transition in InSb, a prototypical example of the narrow-gap III-V semiconductors, using time- and angle-resolved photoemission spectroscopy. The interband transitions below 1.7 eV are correctly described in terms of the one-electron band picture for the whole Brillouin zone. The transitions along the Γ-K line are also described by the one-electron band picture above 1.7 eV, while the transitions along the Λ direction turn out to be excitonic associated with the saddle-point excitons above 1.7 eV. The unique photoemission peak, which is resonantly enhanced under excitation at 1.85 eV, has been identified as being caused by the saddle-point excitons in InSb, based on the analysis of time-, energy-, and momentum-resolved spectroscopic features. Using the momentum-resolved capability of photoemission spectroscopy, the IQP Bloch states of which the exciton is composed have been determined for the states along the Γ-L line. Also, using ultrafast time-resolved capability, we have shown that coherently generated excitonic polarization associated with the SPE decay with a time constant of 22 fs, which corresponds to the autoionization processes from the excitons to unbound electron-hole pair states. Therefore, the saddle-point exciton plays an important role at the E_1 critical point even in InSb, which has narrow band-gap energy and a large high-frequency dielectric constant. This work has demonstrated that the time- and angle-resolved photoemission spectroscopy provides far deeper insight into the nature of the excitonic states formed at the high-energy region above the E_G in semiconductors.

ACKNOWLEDGMENTS

We thank K. Nasu, J. Kanasaki, and J. Güdde for valuable discussions. This work was supported by the Japan Society for the Promotion of Science (JSPS) KAKENHI Grant No. 24000006.

APPENDIX: TEMPORAL EVOLUTION OF PHOTOEMISSION PEAKS UNDER 1.63-eV EXCITATION

In Figs. 6(a)–6(d), we show temporal changes in the photoemission map under 1.63-eV excitation. As seen in Fig. 6(a), the energy- and momentum-resolved map of photoemission under 1.63 eV at $\Delta t = 30$ fs shows a rich structure. Not only the HH and LH peaks in the Γ valley, but peak A is also excited near the saddle point of the CB along the Γ-L line with the highest intensity. Furthermore, two other peaks, labeled S_1 and S_2, can be resolved in the L valley; they have initial-state energies almost the same as the HH and LH states in the Γ valley, respectively. In order to make clear the origins of these photoemission peaks, we analyze not only energetics but also the relaxation dynamics of these peaks.

In Figs. 6(a)–6(d), it is clear that the intensity of peak A is transferred to peak S_1 substantially during 167 fs, and the peak S_1 is merged with peak S_2 during relaxation. The merged peak is then relaxing toward the low-energy and high-$k_{||}$ sides gaining more intensity at later time delays. The features of relaxation can be well interpreted in terms of relaxation of

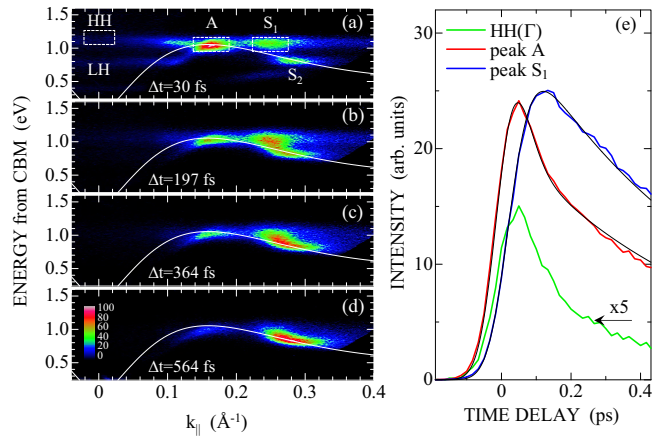

FIG. 6. (a)–(d) Temporal evolution of photoemission images plotted as a function of $k_{||}$ and $E_I(\vec{k})$ under 1.63-eV excitation. Images were measured at Δt indicated in each panel, and intensities are characterized by a common color scale in (d). The solid curve shows the conduction-band dispersion along the Γ-L direction. The rectangles labeled HH, A, and S_1 are the regions where the intensities are integrated for quantitative analysis of their temporal evolutions. (e) Temporal changes of integrated intensities for peak HH (green), A (red), and S_1 (blue). Solid black curves show the results of analysis using a set of rate equations (see the text).

nonthermal electrons in the L valley of CB, as studied extensively in Ref. [35].

In Fig. 6(e), we plot temporal changes in intensities of peaks A, S_1, and HH, which were obtained by integrating the intensities within the rectangles shown in Fig. 6(a). It is clear that the rise of peak A is as fast as that of peak HH, and precedes that of peak S_1, showing that peak A, as well as peak HH, is the primary state of photoexcitation and that peak S_1 is due to a secondary state generated as a result of relaxation. In order to quantify the correlation between peaks A and S_1, we analyze quantitatively temporal changes in intensities using a set of rate equations to describe temporal changes in the populations which are correlated with each other. For the population n_A for the peak A and n_S for the peak S_1,

$$\frac{dn_A}{dt} = I_{\text{pump}}\exp\{-(t/w)^2\} - k_{AS}n_A + k_{SA}n_S, \tag{A1}$$

$$\frac{dn_S}{dt} = k_{AS}n_A - (k_{SA} + k_S)n_S, \tag{A2}$$

where k_{AS} (k_{SA}) is the rate of population conversion from peak A to S_1 (S_1 to A), and k_S is the rate of energy relaxation from peak S_1 to lower states. Importantly, the above equations assume that the photoexcitation does not generate directly the state responsible for peak S_1. The thin solid black curves in Fig. 6(e) are the results of calculations of the above set of rate equations with the following parameters: $w = 62.5$ fs, $k_{AS} = 25.6 \times 10^{12}\ \text{s}^{-1}$, $k_{SA} = 11.4 \times 10^{12}\ \text{s}^{-1}$, and $k_S = 2.5 \times 10^{12}\ \text{s}^{-1}$. The calculated results fit reasonably well to the temporal changes in intensities of peak A and peak S_1. In the analysis above, possible roles of peak HH were neglected for simplicity, as the intensity of peak HH is much weaker than that of peaks A and S_1.

The results and analysis described above have shown clearly that peak A is due to the primary state of 1.63-eV photoexcitation, and that peak S_1 is due to the secondary state populated by the transformation from the primary state. Similar analysis for peak S_2 and the peak labeled LH in the Γ valley has shown that peak S_2 is due to the secondary state transferred from the primary state responsible for peak LH. For photoemission peaks observed under different photon energies, similar analysis of the rise times has been carried out to identify the primary-state photoemissions. All photoemission peaks due to secondary states are labeled S in Figs. 1, 2, and 6.

[1] P. Y. Yu and M. Cardona, *Fundamentals of Semiconductors: Physics and Materials Properties* (Springer, Berlin, 1996).

[2] Y. Toyozawa, *Optical Processes in Solids* (Cambridge University Press, New York, 2003).

[3] J. C. Phillips, Phys. Rev. **136**, A1705 (1964).

[4] J. C. Phillips and B. O. Seraphin, Phys. Rev. Lett. **15**, 107 (1965).

[5] S. W. Koch, M. Kira, G. Khitrova, and H. M. Gibbs, Nat. Mater. **5**, 523 (2006).

[6] J. Shah, *Ultrafast Spectroscopy of Semiconductors and Semiconductor Nanostructures* (Springer, Berlin, 1999) [second edition].

[7] V. M. Axt and T. Kuhn, Rep. Prog. Phys. **67**, 433 (2004), and references therein.

[8] F. Rossi and T. Kuhn, Rev. Mod. Phys. **74**, 895 (2002).

[9] E. O. Kane, Phys. Rev. **180**, 852 (1969), and references therein.

[10] D. E. Aspnes and A. A. Studna, Phys. Rev. B **7**, 4605 (1973).

[11] S. F. Pond and P. Handler, Phys. Rev. B **8**, 2869 (1973).

[12] P. Lautenschlager, M. Garriga, S. Logothetidis, and M. Cardona, Phys. Rev. B **35**, 9174 (1987).

[13] P. Lautenschlager, M. Garriga, L. Vina, and M. Cardona, Phys. Rev. B **36**, 4821 (1987).

[14] J. C. Phillips, Excitons, in *The Optical Properties of Solids*, edited by J. Tauc (Academic, New York, 1966), pp. 155–184.

[15] U. Fano, Phys. Rev. **124**, 1866 (1961).

[16] K. F. Mak, J. Shan, and T. F. Heinz, Phys. Rev. Lett. **106**, 046401 (2011).

[17] K. F. Mak, F. H. da Jornada, K. He, J. Deslippe, N. Petrone, J. Hone, J. Shan, S. G. Louie, and T. F. Heinz, Phys. Rev. Lett. **112**, 207401 (2014).

[18] W. Hanke and L. J. Sham, Phys. Rev. Lett. **43**, 387 (1979).

[19] L. X. Benedict, E. L. Shirley, and R. B. Bohn, Phys. Rev. B **57**, R9385 (1998).

[20] M. Rohlfing and S. G. Louie, Phys. Rev. B **62**, 4927 (2000), and references therein.

[21] L. Chiodo, J. M. García-Lastra, A. Iacomino, S. Ossicini, J. Zhao, H. Petek, and A. Rubio, Phys. Rev. B **82**, 045207 (2010).

[22] A. Riefer, F. Fuchs, C. Rödl, A. Schleife, F. Bechstedt, and R. Goldhahn, Phys. Rev. B **84**, 075218 (2011).

[23] R. J. Elliott, Phys. Rev. **108**, 1384 (1957).

[24] H. Ohnishi, N. Tomita, and K. Nasu, Int. J. Mod. Phys. B **32**, 1850094 (2018).

[25] H. Tanimura and K. Tanimura, Phys. Rev. B **102**, 045204 (2020).

[26] E. Perfetto, D. Sangalli, A. Marini, and G. Stefanucci, Phys. Rev. B **94**, 245303 (2016).

[27] A. Rustagi and A. F. Kemper, Phys. Rev. B **97**, 235310 (2018).

[28] D. Sangalli, E. Perfetto, G. Stefanucci, and A. Marini, Eur. Phys. J. B **91**, 171 (2018).

[29] A. Rustagi and A. F. Kemper, Phys. Rev. B **99**, 125303 (2019).

[30] I. Vurgaftman, J. R. Meyer, and L. R. Ram-Mohan, J. Appl. Phys. **89**, 5815 (2001).

[31] T. J. Kim, S. Y. Hwang, J. S. Byun, M. S. Diware, J. Choi, H. G. Park, and Y. D. Kim, J. Appl. Phys. **114**, 103501 (2013).

[32] Landolt-Börnstein, in *Semiconductors*, edited by O. Madelung, M. Schulz, and H. Weiss (Springer, Berlin, 1982), Vols. 17a and 17b.

[33] K. L. Shaklee, J. E. Rowe, and M. Cardona, Phys. Rev. **174**, 828 (1968).

[34] J. Kanasaki, H. Tanimura, and K. Tanimura, Phys. Rev. Lett. **113**, 237401 (2014).

[35] H. Tanimura, J. Kanasaki, and K. Tanimura, Phys. Rev. B **91**, 045201 (2015).

[36] K. Oura, V. G. Lifshits, A. A. Saranin, A. V. Zotov, and M. Katayama, *Surface Science: An Introduction* (Springer, Berlin, 2003).

[37] W. Mönch, *Semiconductor Surfaces and Interfaces* (Springer, Berlin, 1995).
[38] M. Weinelt, M. Kutschera, R. Schmidt, C. Orth, T. Fauster, and M. Rohlfing, Appl. Phys. A **80**, 995 (2005).
[39] E. W. Plummer and W. Eberhardt, *Advances in Chemical Physics* (Wiley, New York, 1982).
[40] Y.-S. Kim, M. Marsman, G. Kresse, F. Tran, and P. Blaha, Phys. Rev. B **82**, 205212 (2010).
[41] B. D. Malone and M. L. Cohen, J. Phys.: Condens. Matter **25**, 105503 (2013).
[42] A. Damascelli, Z. Hussain, and Z.-X. Shen, Rev. Mod. Phys. **75**, 473 (2003).
[43] S. I. Pekar, Sov. Phys. Solid State **4**, 953 (1962).
[44] D. S. Chemla, J.-Y. Bigot, M.-A. Mycek, and S. Weiss, and W. Schäfer, Phys. Rev. B **50**, 8439 (1994).
[45] B. Krömker, M. Escher, D. Funnemann, D. Hartung, H. Engelhard, and J. Kirschner, Rev. Sci. Instrum. **79**, 053702 (2008).
[46] H. Haug and S. W. Koch, *Quantum Theory of the Optical and Electronic Properties of Semiconductors* (World Scientific, Singapore, 1990).
[47] The semiconductor Bloch equations have to be supplemented with an appropriate treatment of the complicated scattering terms involved in pulse excited semiconductors. Unfortunately, we were unable to obtain the details of the scattering processes under the present temporal and energy resolutions of the measurements. Also, the dephasing process of coherent excitonic polarization formed above the E_G is influenced by a strong interaction with a continuum of unbound electron-hole pair states, resulting in completely different mechanisms of dephasing from those of the Γ excitons formed at energies below the E_G. How to describe the dephasing process of high-energy excitonic polarization is not trivial. Here we use a simple optical Bloch equation neglecting all Coulomb interaction terms in the semiconductor Bloch equations; we obtain only phenomenological quantities of population decay time T_1 and polarization dephasing time T_2.
[48] T. Hertel, E. Knoesel, M. Wolf, and G. Ertl, Phys. Rev. Lett. **76**, 535 (1996).
[49] P. C. Becker, H. L. Fragnito, C. H. Brito Cruz, R. L. Fork, J. E. Cunningham, J. E. Henry, and C. V. Shank, Phys. Rev. Lett. **61**, 1647 (1988).
[50] X. Cui, C. Wang, A. Argondizzo, S. Garrett-Roe, B. Gumhalter, and H. Petek, Nat. Phys. **10**, 505 (2014).
[51] V. M. Silkin, P. Lazić, N. Došlić, H. Petek, and B. Gumhalter, Phys. Rev. B **92**, 155405 (2015).
[52] R. Huber, F. Tauser, A. Brodschelm, M. Bichler, G. Abstreiter, and A. Leitenstorfer, Nature **414**, 286 (2001).
[53] A. Leitenstorfer, R. Huber, F. Tauser, and A. Brodschelm, Phys. Status Solidi B **238**, 455 (2003).
[54] This assumption may overestimate the plasma density, as the major fraction of absorbed photons excites the coherent excitonic polarization, not unbound electron-hole pairs. As seen in Fig. 3(c), the EX photoemission intensity is 5 times higher than that of the total intensity of conduction electrons at 1.85 eV. If we assume that the intensity ratio represents the ratio of yields of excitonic polarization and unbound electron-hole pairs, then the plasma density is about 20% of ρ_0. Consequently, $2\pi/\omega_{pl}$ changes from 83 to 165 fs, which is substantially longer than the T_1. This could be a reason why the magnitude of T_1 does not depend on ρ_0.